Longitudinal deep-brain imaging in mouse using visible-light optical coherence tomography through chronic microprism cranial window

Lisa Beckmann,[1,7] **Xian Zhang,**[1,2,7] **Neil A. Nadkarni,**[4] **Zhen Cai,**[1,2] **Ayush Batra,**[4] **David P. Sullivan,**[3] **William A. Muller,**[3] **Cheng Sun,**[5] **Roman Kuranov,**[1,6] **and Hao F. Zhang**[1,*]

[1] *Department of Biomedical Engineering, Northwestern University, Evanston IL 60208, USA*
[2] *Department of Ophthalmology, Tongji Hospital, Tongji Medical College, HuaZhong University of Science and Technology, Wuhan, Hubei, China*
[3] *Department of Pathology, Northwestern University, Chicago IL 60611, USA*
[4] *Department of Neurology, Northwestern University, Chicago IL 60611, USA*
[5] *Department of Mechanical Engineering, Northwestern University, Evanston IL 60208, USA*
[6] *Opticent Health, Evanston IL, Evanston IL 60201, USA*
[7] *These authors contributed equally to this work*
[*] *hfzhang@northwestern.edu*

Abstract: We longitudinally imaged both the superficial and deep cortical microvascular networks in brains of healthy mice and in a mouse model of stroke *in vivo* using visible-light optical coherence tomography (vis-OCT). We surgically implanted a microprism in mouse brains sealed by a chronic cranial window. The microprism enabled vis-OCT to image the entire depth of the mouse cortex. Following microprism implantation, we imaged the mice for 28 days and found that that it took around 15 days for both the superficial and deep cortical microvessels to recover from the implantation surgery. After the brains recovered, we introduced ischemic strokes by transient middle cerebral artery occlusion (tMCAO). We monitored the strokes for up to 60 days and observed different microvascular responses to tMCAO at different cortical depths in both the acute and chronic phases of the stroke. This work demonstrates that the combined microprism and cranial window is well-suited for longitudinal investigation of cortical microvascular disorders using vis-OCT.

1. Introduction

Stroke is the second leading cause of death globally and the third leading cause of premature death and disability [1]. Given that a significant proportion of patients who suffer from stroke survive, research efforts have been prioritized towards either expedient treatment or neurorehabilitation. Neovascularization, the formation of new capillaries from blood vessels, has been considered a target of interest for neurorehabilitation [2]. The neurovascular unit (NVU) is the basic building block, from which angiogenesis can proceed. In contrast to commonly used post-mortem studies, *in vivo* longitudinal imaging of the vasculature in preclinical models provides a unique opportunity to study the physiologic progression of neovascularization. However, *in vivo* investigations have heavily relied on multi-photon microscopy, which requires repeated use of extrinsic fluorescent labels [3,4].

Visible-light optical coherence tomography (vis-OCT) is a three dimensional (3D), anatomical and functional imaging modality with microscopic resolution. Using visible light illumination, vis-OCT offers higher axial resolution and is more sensitive to differences in oxygenated and deoxygenated hemoglobin absorptions compared to traditional near-infrared OCTs [5].

These characteristics of vis-OCT have been applied extensively to investigate retinal anatomy, vasculature, and metabolic rate of oxygen in both rodents and humans [6–14]. Vis-OCT has also been applied to brain imaging for functional and structural evaluations [15–20]. For example, Liu *et al.* [20] and Chen *et al.* [15] quantified acute changes in oxygen saturation in superficial vessels in the mouse cortex following ischemic stroke. Srinivasan *et al.* [19] imaged mice for one week following ischemic stroke, measuring various parameters including blood flow, vessel diameter, and capillary density. In all these studies, vis-OCT enabled measurements of *in vivo* cerebrovascular dynamics with label-free visualization of blood flow, eliminating the need for extrinsic fluorescent labels.

Despite the above-mentioned unique advantages, all reported vis-OCT *in vivo* brain studies had two major limitations. First, the imaging depth was limited to ~200–400 μm due to the relatively high attenuation of visible light in the brain, making it difficult to image the deep cortex [21]. Second, the duration of the reported studies is limited to one week following induction of strokes, although vessel remodeling continues for 60 days post-stroke [22–24].

Microprism implantation with a chronic cranial window into the brain has previously been used in other optical microscopy modalities (e.g., two-photon microscopy, confocal microscopy, and epi-fluorescence microscopy) for deep brain imaging. These studies demonstrated that the addition of microprism caused manageable neural damages while dramatically expanding the capability to investigate deep brain and still allowing longitudinal observation of the brain [25–28]. Therefore, microprism implantation can potentially benefit vis-OCT for deep-brain imaging to circumvent the strong visible light attenuation in the brain.

In this study, we integrated the microprism with vis-OCT in the brain to facilitate high-resolution imaging of the deeply penetrating vascular network in the cortex. We also tracked the structural and functional vascular responses to the microprism implantation, which informed us of the brain recovery time from implantation surgery. In addition, we longitudinally monitored mice after transient middle cerebral artery occlusion (tMCAO), a widely used model for ischemic stroke, for up to two months after the day of stroke. These studies will pave the way for future investigations of the vascular mechanisms of ischemic stroke recovery.

2. Methods

2.1. Experimental setup

We developed a vis-OCT microscope system for brain imaging (Fig. 1). The schematic of this system is shown in Fig. 1(a). We used light from a supercontinuum laser (SuperK EXTREME EXW-6, NKT Photonics) after passing through a short pass filter (Semrock FF02-694) as the light source. We used a 30:70 fiber coupler (Gould Fiber Optics). In the sample arm, a pair of galvanometer scan mirrors (QS-7, Nutfield Technology) routed the beam through a scan lens (LSM03-VIS, Thorlabs) with an effective focal length of 39 mm. The illumination beam diameter was 4 mm before being focused onto the sample. The incident light power was 1.4 mW. We estimated the numerical aperture to be about 0.05, resulting in a theoretical lateral resolution of 6.8 μm in air. We used a commercial spectrometer (Blizzard SR, Opticent Health), which covers the spectral range from 510 nm to 614 nm. Typical spectra from the reference are and the sample arm spectra are shown in Fig. 1(b). These spectra fall between Gaussian and rectangular profiles. The weighted center wavelength λ_c is 564 nm. For a Gaussian spectral profile, the theoretical axial resolution δz in air is 1.4 μm as given by $\delta z_{Gauss} = \frac{0.44\lambda_c^2}{\Delta\lambda}$ [29]. For a rectangular spectral profile, the theoretical axial resolution in air is 1.9 μm as given by $\delta z_{Rect} = \frac{0.60\lambda_c^2}{\Delta\lambda}$. Our experimentally measured axial resolution in air was 1.8 μm (Fig. 1(c)), which is between the theoretical axial resolutions for Gaussian and rectangular spectral profiles. Assuming a tissue refractive index n = 1.37 [30], our axial resolution in brain tissue is 1.3 μm. We used a silver mirror as a sample for both axial resolution and sensitivity roll-off measurements. Figure 1(d)

shows the measured sensitivity as a function of scanning depth at a step size of ~75 μm. The maximum SNR of 95 dB was measured at 75 μm from the zero-delay line. The system sensitivity roll-off was measured to be 4.5 dB/mm in air.
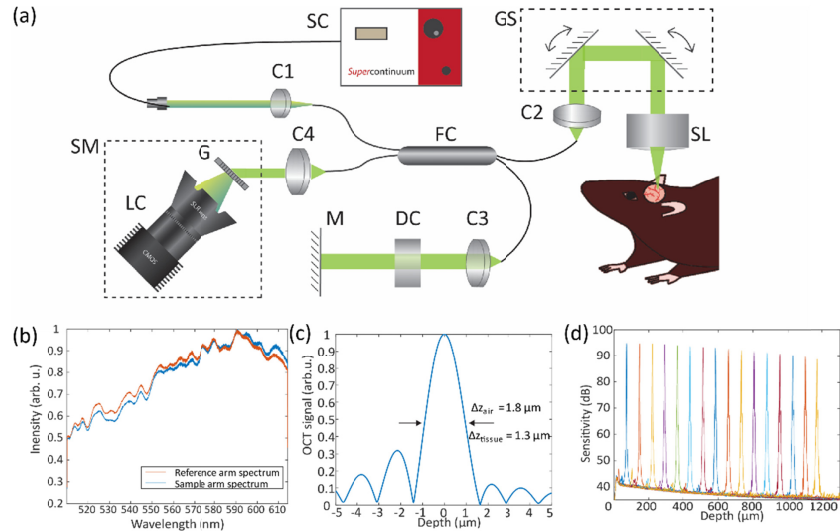

Fig. 1. (a) Schematic of the experimental vis-OCT system. C: collimator; CL: camera lens; DC: dispersion compensation; FC: fiber coupler; G: grating; GS: galvanometer scanners; LC: line camera; M: mirror; SC: supercontinuum; SL: scan lens; SM: spectrometer. (b) Reference arm and sample arm spectra. (c) Fourier transform of the spectrum. (d) Sensitivity roll-off.

2.2. Microprism assembly and implantation

Figure 2(a) illustrates the microprism cranial window assembly. We glued two circular coverslips (5-mm-diameter and 8-mm-diameter) concentrically and glued a 1-mm right angle aluminum coated microprism (86–621, Edmund Optics) to the 5-mm-diameter coverslip. We used ultraviolet curing optical adhesive (Norland Optical Adhesive 81) to glue all the parts. The prism is 1-mm deep and penetrates the entire cortex and part of the white matter. Figure 2(b) shows the relationship between the top-view and side-view images with respect to the entire cranial window. We acquired the top-view image via raster-scanning the optical focal spot through the cranial window along the *x–y* plane (Fig. 2(c)). To acquire the side-view image, the vis-OCT illumination beam was reflected by the hypotenuse and imaged through the vertical leg of the prism, where the raster-scanning was translated to the *y-z* plane (Fig. 2(d)). In contrast to previously reported cortical imaging, which only focused on the superficial area of the brain (top-view image), using the prism provides an additional 1000 μm ×750 μm ×250 μm deep cortical volume (Fig. 2(e)).

2.3. Animal preparation

We used four adult wild-type C57BL/6 mice around three months old and 28-35 g for all the experiments. We kept the mice in the Center for Comparative Medicine at Northwestern University under normal lighting conditions with 12-h on and 12-h off cycles. We anesthetized the mice via intraperitoneal injection (10 ml/kg body weight) of a ketamine/xylazine cocktail (ketamine: 11.45 mg/ml; xylazine: 1.7 mg/ml, in saline). Anesthesia depth was monitored via toe pinch test every 15 minutes. Half doses of the ketamine/xylazine cocktail were delivered as needed. During imaging, we maintained their body temperatures by a heating lamp. We used a
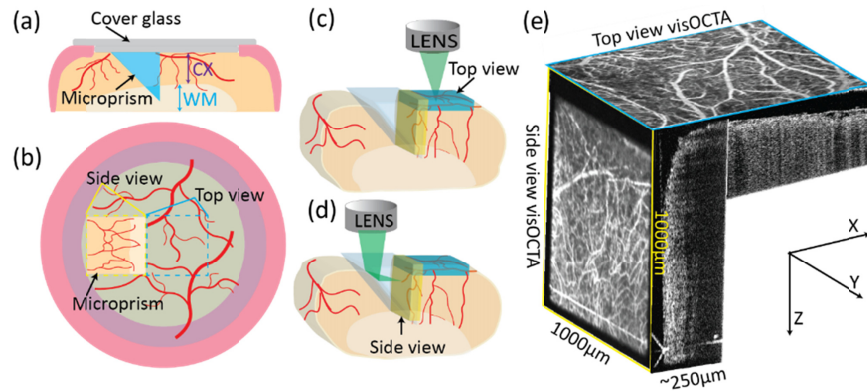
Fig. 2. (a) Schematic of the cranial window-microprism assembly and implantation. CX: cortex; WM: white matter; (b) Relationship between the top-view and side-view images. Yellow dashed square: side-view from the microprism; blue dashed square: top-view; (c) Imaging volume acquired from top-view (blue cuboid); (d) Imaging volume acquired from side-view (yellow cuboid); (e) Illustration of top-view and side-view *en face* vis-OCTA images and B-scan image with respect to their geometries.

pulse oximeter attached to the left rear paw to monitor the peripheral arterial oxygenations and the heart rate.

Our surgical procedures included two steps. First, we created a chronic cranial window with microprism implantation. Second, following a recovery period of at least 15 days, animals underwent tMCAO stroke to investigate microvascular changes within the ipsilateral ischemic hemisphere. After each procedure, we placed the animals in a warm cage for recovery and monitored toe/tail pinch withdrawal, heart rate, respiratory rate, and systemic oxygenation every 20 min until the mice fully recovered. Following stroke, we monitored the health of the mice daily in the first three days following stroke, every 3 days in the following week, and once a week thereafter. Sacrifice criteria were determined by IMPROVE guidelines, which set specific expected symptoms for tMCAO at various time points post-stroke [31]. The stroke was not successful in one mouse, who was immediately sacrificed. Two mice experienced progressive weight loss of more than 20% at over 48 hours post-stroke and did not recovery by 7 days post-stroke; we sacrificed them on the 7th day. One mouse experienced weight loss of 15% but recovered within 7 days post-stroke and remained active and well-groomed throughout the course of follow-up monitoring. This mouse was sacrificed at 60 days post-stroke, in accordance with the end point set in our IACUC protocol. All experimental procedures were approved by the Northwestern University IACUC.

2.4. Protocol for chronic microprism cranial window implantation

Once completely anesthetized, we placed the mice on a custom-built mouse holder. We removed the hair and swabbed the scalp with 70% alcohol 3-5 times to prepare the area. Then we removed the skin to expose the skull. The tissue adhesive (Vetbond, 3M) was pre-smeared on the top of skull and muscle to create a durable flat surface. We performed a 5.5-mm diameter craniotomy on top of the left side of parietal–temporal cortex using a dental drill. We centered the cranial window at 2.5-mm left lateral of midline and 2.0-mm caudal to the bregma. We then carefully removed the dura using a small forcep. Corresponding to the prism location and size, we made a 1 mm × 1 mm incision at the dorsal side using a 27-gauge sharp syringe needle. We then removed brain tissue at the incision site with an approximate volume of the prism to allow for placement and prevent high intracranial pressure post-implantation. The incision was gently

rinsed with sterile artificial cerebrospinal fluid until bleeding ceased. The caudal medial edge of the microprism was aligned adjacent to the centering point of the cranial window. The microprism assembly was then attached under the cranial window with the prism's vertical plane firmly attached to the temporal edge of incision. The outer part of the 8-mm diameter coverglass was glued to the skull using tissue adhesive (Vetbond, 3M), followed by ultraviolet curing optical adhesive to fill any gap between the skin and tissue adhesive. No gross behavioral deficits were noticed in the mice afterwards.

2.5.　tMCAO model

Surgically induced stroke using the Koizumi method [32] was performed after the mice fully recovered from the microprism and chronic window implantation. Following the same anesthesia and disinfection protocol mentioned above, the mice were immobilized in the dorsal position on the surgical plane. Briefly, through a 2-cm midline neck incision, the left common carotid artery (CCA) and external carotid artery (ECA) were sequentially permanently ligated (2-3 mm distal to bifurcation) with 6-0 silk sutures. Permanent ligation was given to the proximal part of the CCA and a vessel clip was placed just after the CCA bifurcation on the internal carotid artery (ICA). An arteriotomy was performed between the permanent CCA suture and the CCA bifurcation and a silicone-coated filament (Doccol 602123) was introduced via the arteriotomy until it reached the vessel clip. The loose collar suture on the internal carotid artery (ICA) was gently tightened around the CCA and the vessel clip was withdrawn. The filament was slowly advanced through the ICA toward the cranial base until it was 9 mm from the bifurcation. The inserted filament remained in place for 60 mins and was gently pulled out to induce transient stroke model with reperfusion achieved by collateral circulation from the Circle of Willis. The wound was closed with interrupted 5-0 silk sutures.

2.6.　Imaging protocols for brain vis-OCT and vis-OCT angiography (vis-OCTA)

Prior to initiation of the stroke model, we monitored the cranial window to assess its quality and stability at days 2, 3, 7, 15, 21, and 28. After the stroke, we imaged the mice continuously for three days, which represented the acute period, at day 7 after stroke, and then imaged the mice on day 30 and day 60 post-stroke, which represented the chronic period.

For monitoring, we consistently acquired images 20-30 minutes after anesthesia induction. During each imaging session, we acquired both top- and side-view images. To acquire vis-OCT images, we scanned 512 B-scans with 512 A-lines per B-scan. The integration time for each A-line was 20 µs. The top-view image covers a 1.8 mm × 1.8 mm area and the side-view image covers a 1.05 mm × 1.05 mm area (limited by the size of the microprism). To acquire vis-OCTA images, we repeated each B-scan 5 times with 512 A-lines per B-scan, which took 26 seconds. To visualize each vis-OCT and vis-OCTA volume as a 2D image, we took a maximum intensity projection of brain tissue. Because of potential edema and liquid above the brain surface, this slab thickness was optimized for each volume to ensure that all vessels in the volume were visible in the *en face* images.

2.7.　Data processing and statistical analysis

We followed the method described by Chen *et al* [15] to process vis-OCTA images and extract hemoglobin oxygen saturation (sO_2). We used ImageJ [33] to overlap two images from the same region of interest (ROI) at different time points, allowing us to qualitatively analyze morphological changes in the imaged vasculature. The degree to which the images overlap can reflect the morphological stability between two different time points. We calculated blood vessel diameter by manually measuring the diameter of the largest blood vessel within the ROI using ImageJ. We repeated this measurement for the same section of the same vessel 5 times at each time point. These results were then averaged to obtain the mean value and standard deviation. We performed

blood vessel density calculations using the AngioTool, which automatically detects the vessels and calculates the vessel area density in the whole tissue [34]. We used the same parameters in AngioTool to measure both top- and side-view images at different time points. We used data from three mice for further statistical analysis. One-way ANOVA analysis and two-tail t-test were used for comparing the vessel density and diameter among the data of different days. For all data, errors are reported as standard error of the mean and $P < 0.05$ was considered statistically significant.

2.8. Cortical layers separation

For cortical layer separation, we considered that the side-view *en face* image covered the entire cortex. We used the technique outlined in Merkle *et al* [35] to identify cortical layers. Briefly, we determined the average cortical layer thickness as a percentage of the total cortex thickness in the approximate location of imaging using the Allen mouse brain atlas [36]. We then combined layers 1-3 and layer 5-6, giving a thickness percentage distribution of 37%:10%:53% for layers 1-3:4:5-6.

3. Results

3.1. Comparison of resolution with / without microprism

We imaged a 1951 Air Force target to quantify the resolution of vis-OCT with and without using the microprism. We glued the target card to the prism using optical glue (Norland Optical Adhesive 81). Under both conditions, the lines in group 6 subsection 3, corresponding to a resolution of 6.2 μm, were clearly distinguished (data not shown).

3.2. Characteristics of vis-OCT and vis-OCTA images

Figure 3 shows both the vis-OCT and vis-OCTA top-view and side-view *en face* images as well as B-scan images. Figure 3(a) is the optical microscopy image of the entire cranial window. Figure 3(b) and Fig. 3(c) are the top-view and side-view optical images as highlighted in Fig. 3(a). The side-view image acquired through the microprism shows comparable image quality with the top-view image, both of which reveal delicate micro-structures of the vascular network. From the side-view image, we can clearly see the white matter (as highlighted in Fig. 3(c)), which suggests that the depth of the entire cortex is fully covered in the side-view image. Figure 3(d) and Fig. 3(e) are top-view and side-view vis-OCT *en face* images, respectively. Figure 3(f) and Fig. 3(g) are top-view and side-view vis-OCTA *en face* images, respectively, where much richer microvascular networks are revealed as compared with the optical microscopy images. The pseudo-color in Fig. 3(f) encodes vessels depth with respect to the brain-glass interface, where few vessels deeper than 167 μm are visible. As a comparison, the side-view image reveals the vascular network structure from the superficial cortex to the deep white matter area (Fig. 3(g)). Figure 3(h) and Fig. 3(I) are the top-view vis-OCT and vis-OCTA B-scan images. The missing information from the top-view images due to the shadow casted by the vessels from the superficial layer can be recovered from the side-view B-scan images (Fig. 3(j) and Fig. 3(k)), which is more suitable for deep brain investigation. By quantitatively analyzing the vessel morphologies from the recorded vis-OCTA image (Fig. 3(I), red arrow), we confirmed that the image depth was extended from ~250 μm to 1000 μm. In vis-OCT B-scan images from both the top-view (Fig. 3(h)) and side-view (Fig. 3(j)), the cortex demonstrates uniform signal intensities while the white matter showed higher backscattering intensity.

3.3. Brain adaptation after microprism implantation

We monitored the brain for 28 days (Fig. 4) after implantation surgery to track the brain's response to the chronic cranial window and microprism. As shown in the optical microscopic images,
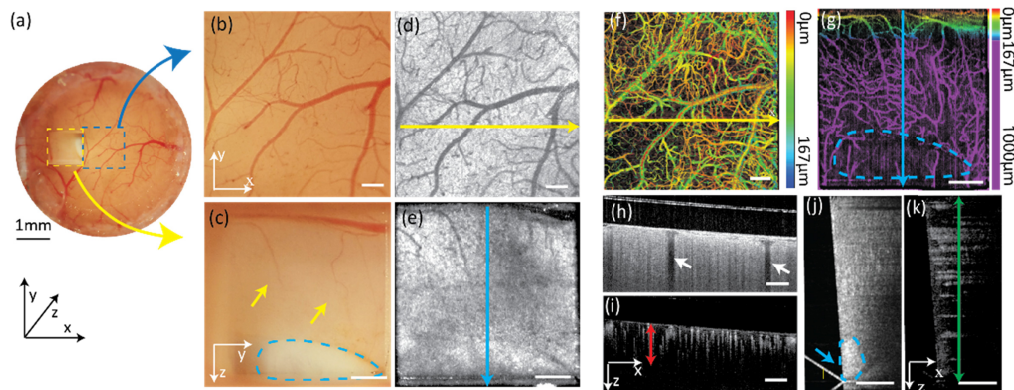
Fig. 3. (a) Optical microscopic image of the entire cranial window with both top-view (blue dash square) and side-view (yellow dash square) from the prism; (b) Magnified optical microscopic image of the area corresponding to the blue dashed area in panel a; (c) Magnified optical microscopic image of the area corresponding to the yellow dashed area in panel a. Yellow arrows: vessels in the deep cortex area; blue dash area: white matter. (d) Top-view *en face* vis-OCT image; (e) Side-view *en face* vis-OCT image; (f) Top-view vis-OCTA image with color-coded vessel depths; (g) Side-view *en face* vis-OCTA image with color-coded vessel depth. Purple area: deep cortex imaged through the prism. Blue dashed area: white matter; (h, i) vis-OCT & vis-OCTA B-scan images acquired from the top-view. White arrows: vessel shadows from top block signal beneath them; Red arrow: effective image depth around 250 μm calculated from the vis-OCTA vessel signal; (j, k) Vis-OCT & Vis-OCTA B-scan images acquired from the side view. green arrow: 1 mm image depth through the prism; blue arrow and dash area: higher backscattering intensity from white matter. (White scale bar: 200 μm).

bleeding was observed on day 2 (Fig. 4(a1)) and day 3 (Fig. 4(a2)), and almost completely absorbed by day 7 (Fig. 4(a3)). The brain cortex remained bleeding free as observed on day 15 (Fig. 4(a4)) and day 28 (Fig. 4(a5)). Vis-OCTA *en face* and Vis-OCT B-scan images reveal greater details than optical microscopy images. The top-view vis-OCTA images on day 2 (Fig. 4(b1)), day 3 (Fig. 4(b2)), and day 7 (Fig. 4(b3)) show dilated vessels (highlighted by the yellow arrows). These vessels recovered by day 15 (Fig. 4(b4)). Vis-OCT B-scan images are from the positions highlighted by the yellow lines in each top-view vis-OCTA *en face* images. The B-scans revealed fluid accumulation between the coverslip and brain both on day 3 (Fig. 4(c2)) and day 7 (Fig. 4(c3)) as highlighted by the blue stars. The fluid was fully resorbed by day 15 (Fig. 4(c4)) and did not recur on day 28 (Fig. 4(c5)).

From the side-view vis-OCTA images, the deep brain showed a lack of flow signal in the first 3 days due to cutting through the cortex (Fig. 4(d1) and Fig. 4(d2), highlighted by the yellow stars). Microvessels started to regenerate as observed on day 7 (Fig. 4(d3)) and stabilized after day 15 (Fig. 4(d4) and Fig. 4(d5), highlighted by the red stars). Like those observed in the top-view vis-OCTA images, vessels in the side-view images showed dilation in the first 7 days and began to shrink thereafter. From the vis-OCT B-scan images, we observed stronger tissue attenuation within certain areas on day 2 (Fig. 4(e1)) and day 3 (Fig. 4(e2)), and mild liquid accumulation on day 7 (Fig. 4(e3)), both of which recovered by day 15 (Fig. 4(e4)). In addition, starting from day 15, we can clearly distinguish the cortex from the white matter based on elevated backscattering as shown in Fig. 4e4 and Fig. 4(e5).

We analyzed vessel stabilization over 28 days after microprism implantation (Fig. 5). For both the top-view and side-view vis-OCTA, we overlaid the images from day 15 and day 28 such that the parts in common between the two images appear yellow. The high degree of overlapping in
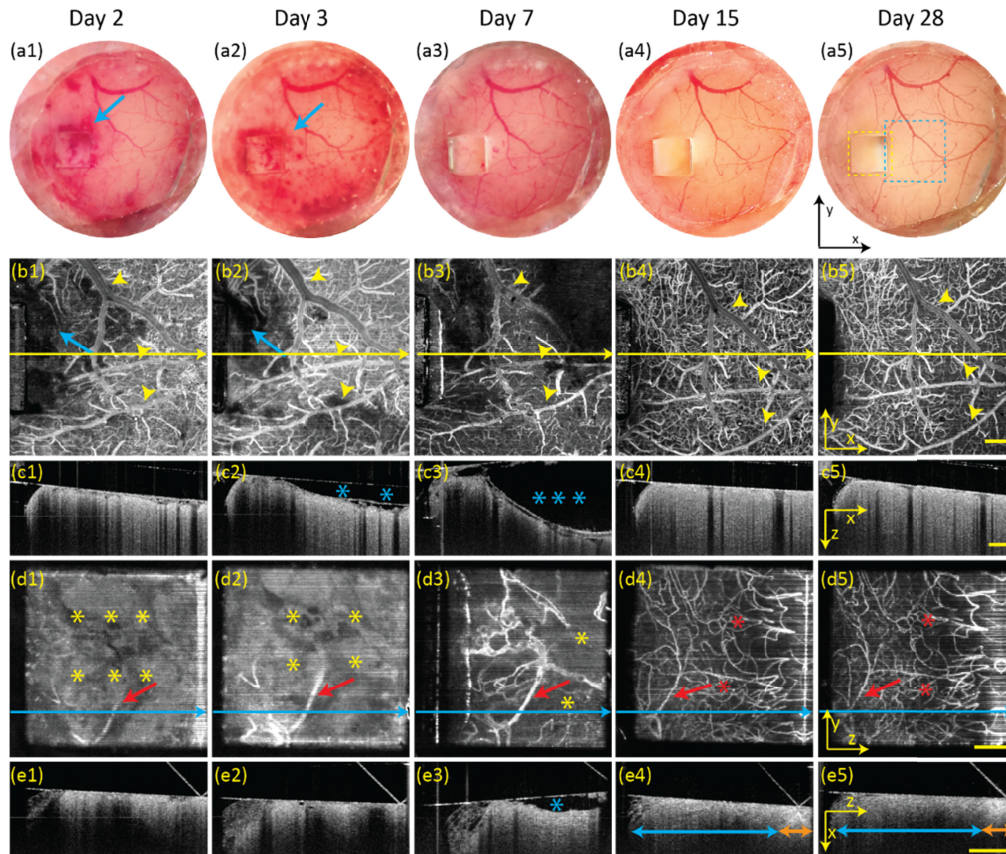
Fig. 4. Longitudinal monitoring of the structure and circulatory change after surgical implantation of the microprism and cranial window from day 2 to day 28. (a1-a5) Optical microscopic images from top-view after implantation. Blue arrows: bleeding; (b1-b5) Top-view vis-OCTA *en face* images acquired from. Blue arrows: bleeding. Yellow arrow heads: vessel diameter variation; Yellow-line: B-scan image positions; (c1-c5) Vis-OCT B-scan images of superficial cortex. Blue stars: liquid accumulation between the brain tissue and cranial window; (d1-d5) Side-view vis-OCTA *en face* images. Yellow stars: non-vascular area; Red stars: vessel reappearance; Red arrows: diameter variation of the same vessel; Blue lines: B-scan positions; (e1-e5) Vis-OCT B-scan images of deep cortex; Blue stars: liquid accumulation between the brain tissue and prism; Blue arrows: full depth of cortex; Orange arrows: white matter. Yellow scale bar: 200 μm.

Fig. 5(a) and Fig. 5(b) shows qualitatively that minimal changes in vessel morphology occurred after day 15 when the brain became stable and adapted to the microprism.
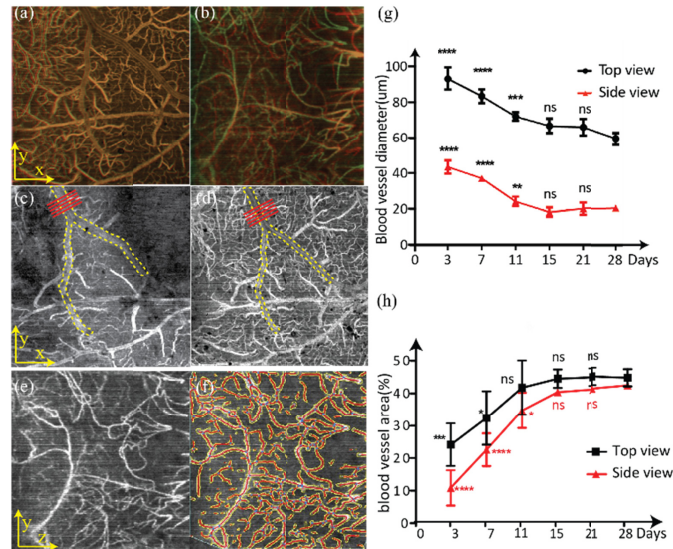

Fig. 5. Determining blood vessel stability using vessel morphology, diameter, and density. (a) Overlaid top-view vis-OCTA en face images from day 15 and day 28; (b) Overlaid side-view vis-OCT en face images from day 15 and day 28. Yellow color: overlapped regions. (c) Top-view vis-OCT image from day 3; (d) Top-view vis-OCT image from day 15. The yellow dashed lines highlight the main vessel within the field of view. The red lines highlight where vessel diameters were measured; (e) Side-view vis-OCTA image on day 11; (f) Vessel segmentation using AngioTool. Yellow: boundaries of automatically detected vessels. Red: centerlines of vessels; (g) Changes in vessel diameters from day 3 to day 28 from both top-view and side-view vis-OCTA images. Mean and standard deviations are plotted. (h) Changes in vessel area density from day 3 to day 28 from both top-view and side-view vis-OCTA images. Mean and standard deviations are plotted. Statistical analysis is compared with Day 28. ns: no significant difference. *: $P < 0.05$, **: $P < 0.01$, ***: $P < 0.001$, ****: $P < 0.0001$.

We further measured the diameter variation of the largest vessel segment in both the top-view and side-view vis-OCTA image over 28 days. Figure 5(c) and Fig. 5(d) show how we measured the vessel diameter between two time points. We measured a single identified vessel segment in each field of view manually five times from positions highlighted by the red lines and repeated this process at each time point. Figure 5(e) shows the vis-OCTA side-view image on day 11 and Fig. 5(f) shows the corresponding segmented vessels (vessel skeleton in red and vessel boundary in yellow). Figure 5(g) shows the variations in vessel diameters measured from identified vessel segments from both top-view and side-view images over 28 days in one mouse, where identified vessels remained significantly dilated until day 11 and stabilized by day 15. In addition, we calculated vessel area density, defined as the ratio between the total segmented vessel area (in pixels) and the total image area (in pixels). Figure 5(h) shows the variation in vessel area densities averaged for three mice over 28 days. Overall, the area density of deep cortical vessels imaged by the side-view vis-OCTA appeared to be affected more than the superficial vessels imaged by the top-view vis-OCTA. This decrease in vessel area densities immediately followed the microprism implantation and recovered over the following days. The superficial vessels became relatively stable on day 11 while the deep vessels became stable on day 15.

After confirming that the brain adapted after 15 days, we monitored the mice for up to day 60 after stroke to validate that the cranial window and microprism are suitable for long-term investigation. With the complete optical assembly mounted on the head, the mice showed normal behavior. The brain did not exhibit signs of infection and had only minor inflammation and bleeding during the first few days as mentioned above. By day 60, the window and glue remained stably fixed on the head, and the image qualities from both the top and side view exhibited good consistency in optical microscopy, vis-OCT, and vis-OCTA.

3.4. Monitoring tMCAO in mouse

We monitored both acute and chronic changes after tMCAO using vis-OCTA and observed the ischemic and vascular behavior of both the superficial and deep vascular beds (Fig. 6). During the acute period, the vis-OCTA images from the top and side views showed different vascular involvement. Figure 6(a1)–6(a6) are optical microscopic images through the cranial window, Fig. 6(b1)–6(b6) are top-view vis-OCTA images, and Fig. 6(c1)–6(c6) are side-view vis-OCTA images. Compared to vis-OCTA images before stroke (Fig. 6(b1) and Fig. 6(c1)), severe reduction of capillary density was observed in the side-view image (Fig. 6(c2)) on day 1 while the capillary density in the top-view image (Fig. 6(b2)) was only slightly affected. However, on day 2, the vessel density from the side-view image (Fig. 6(c3)) increased, demonstrating reperfusion in the deep cortex. Meanwhile, a decrease in vessel density appeared in the top-view image on day 2 (Fig. 6(b3)). On day 3, reperfusion can be seen from both top-view (Fig. 6(b4)) and side-view images (Fig. 6(c4)). In addition, we observed vessel dilation in both the top-view (highlighted by the blue arrows) and side-view images (highlighted by the green arrows) in the first 3 days.
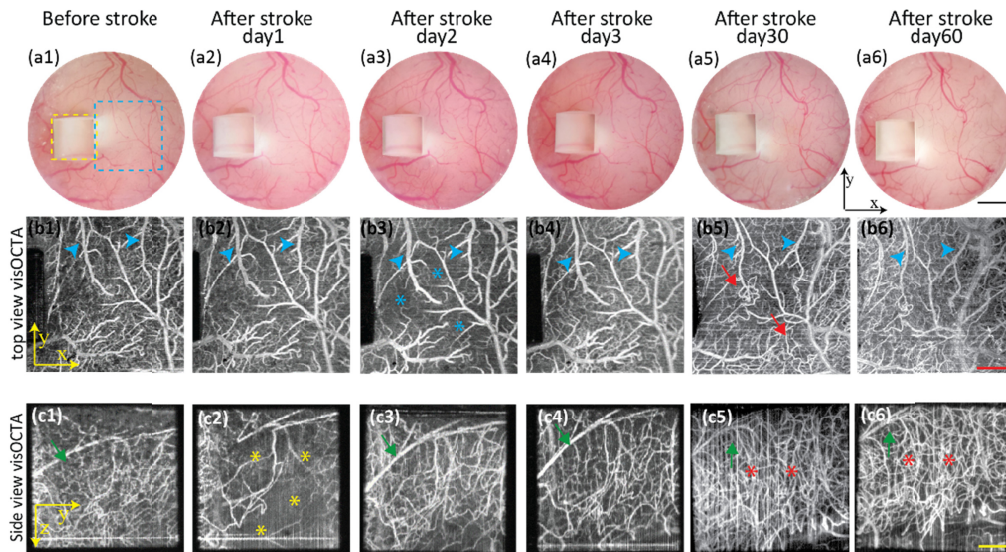

Fig. 6. Longitudinal monitoring of acute (day 1 to day 3) and chronic (day 30 and day 60) changes after tMCAO. (a1-a6) Optical microscopic images from top-view before and after tMCAO. Yellow dashed square: side view from the microprism; blue dashed square: top-view; (b1-b6) Top-view vis-OCTA *en face* images before and after tMCAO. Blue arrow heads: vessel dilation (b2-b4); vessel constriction (b5-b6). Blue stars: reduced flow signal. Red arrows: bounded neovascularization. (c1-c6) Side-view vis-OCTA *en face* images before and after tMCAO. Green arrows: vessel dilation (c3-c4); vessel narrowing (c5-c6). Yellow stars: reduced flow signal. Red stars: overgrown neovascularization. (Black scale bar: 1mm; Red scale bar: 400 µm, Yellow scale bar: 200 µm)

On day 30 and day 60, which represented the chronic stage after stroke, no non-perfused regions were observed from both the superficial and deep cortex. In both the top-view and side-view images, major vessel diameters (highlighted by the blue green arrows) shrunk in the chronic stage as compared to baseline prior to and acutely after stroke. We observed vessel deformation in the top-view image (Fig. 6(b5) and Fig. 6(b6), highlighted by the red arrows). Side-view vis-OCTA images revealed the disappearance of a large vessel in the deeper cortex, which was replaced by a robust increase in vessel density (Fig. 6(c5) and Fig. 6(c6), highlighted by the red stars). Additionally, we note that the field of view through the side view shifted from day to day, most notably between day 3 and day 30. This shift corresponds to a roughly 200 µm lateral shift. We speculate that this change can be caused by anatomcial alterations following stroke outside the field of view. Increased cavity size or change in ventricle size could cause distortion of the brain, accounting for this difference in field of view [37,38].

Using the side-view vis-OCTA *en face* images, we analyzed vascular changes during the first week following stroke (Fig. 7). Figure 7(a) shows an example of a side-view vis-OCTA *en face* image divided into three cortical layer groups covering layers 1-3, 4, and 5-6 [39]. The blood vessel area density over the first week following stroke is plotted for each cortical layer group in Fig. 7(b). Before stroke, vessel density is highest in layer 4. For both the most superficial group (layers 1-3) and layer 4, a clear decrease in vessel density from the baseline to day 3 post stroke
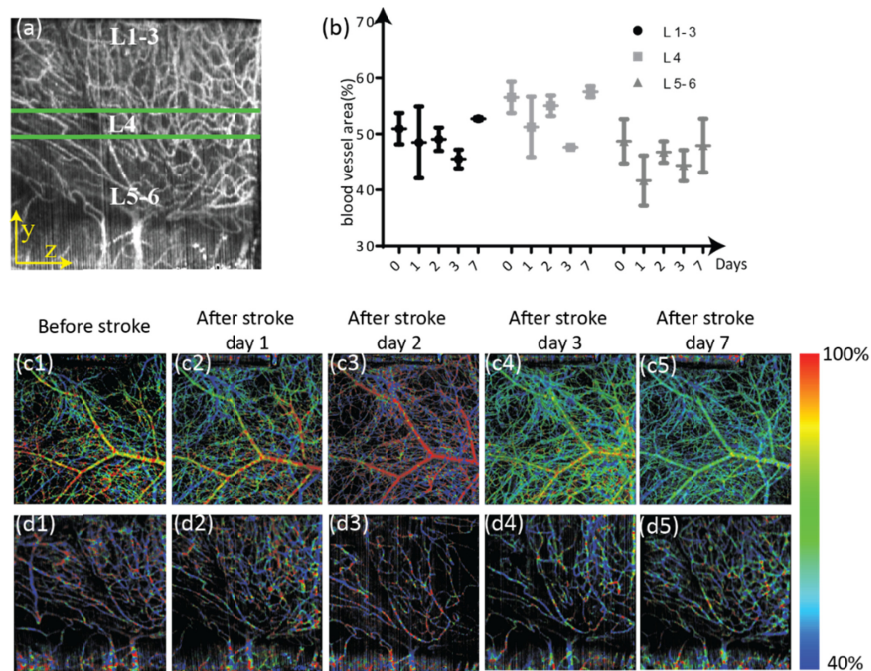

Fig. 7. Vascular changes during the first week after stroke. (a) Side-view vis-OCTA *en face* image showing the cortical layer separations, with the three layer groups highlighted by the green horizontal lines. L1-3: layers 1-3 of the cortex; L4: layer 4 of the cortex; L5-6: layers 5 and 6 of the cortex. (b) Changes in vessel density from day 0 (acquired immediately before performing the stroke) to day 7 after the stroke, separated by cortical layer groups. Mean and standard deviation across three mice are plotted. (c1-c5) Top-view vis-OCTA *en face* images pseudo-colored according to measured sO_2, from immediately before stroke to 7 days after stroke. (d1-d5) Side-view vis-OCTA *en face* images pseudo-colored according to measured sO_2, from immediately before stroke to 7 days after stroke.

can be observed. Such a decrease in vessel density is remedied by day 7 after stroke. The most significant decrease in vessel density occurs on day 2 after stroke in layers 5-6; the change in vessel density is again remedied by day 7 after stroke. Figures 7(c1)–7(c5) and 7d1–7(d5) show vis-OCTA *en face* images pseudo-colored according to sO_2 values for the top-view and side-view, respectively. In day 2 after stroke, the large superficial vessel of the top-view image shows an increase in sO_2 (Fig. 7(c3)). However, this increase appears limited to only that particular vessel within the field of view, with the smaller and deeper vessel appearing less oxygenated than in the baseline and day 1 post stroke (Fig. 7(c3) compared to Figs. 7(c1)–7(c2)). The vessel density in the side-view image on day 2 post-stroke is reduced, but the sO_2 does not appear to be significantly changed (Fig. 7(d3) compared to Figs. 7(d1)–(d2)). In the top-view image, day 3 post-stroke sO_2 appears much more similar to baseline than day 2 post-stroke (Fig. 7(c4) compared to Fig. 7(c1)). However, by day 7, the main vessel in the top-view image appears less oxygenated when compared with all the prior time points (Fig. 7c5). Additionally, at day 7, the entire pseudo-colored image appears muted, with little oxygen saturation contrast between different vessels, possibly implying that less oxygen is being extracted (Fig. 7(c5)). Starting on day 3 post-stroke and in day 7 post-stroke on the side-view images, a greater number of vessels with intermediate sO_2 levels than in the baseline image (Figs. 7(d4)–7(d5)) can be observed.

4. Discussion

Despite the great potential in cortical imaging using vis-OCT, reported results are confined to limited imaging depth caused by stronger visible light attenuation in the brain [40]. Although superficial and deep cortical blood vessels can be identified from the depth map in the top-view vis-OCTA images (Fig. 3f), the image quality of those deep cortical vessels decreased tremendously. By integrating the cranial window with a microprism in this study, we extended vis-OCTA to an additional 1000 μm × 750 μm × 250 μm imaging volume (Fig. 2d), which covers the entire cortex and part of the white matter. The side-view images acquired through the microprism clearly visualize the vertical vascular network from the superficial to deep cortex and reveal different patterns compared to the superficial vessels. Therefore, microprism implantation circumvents tissue scattering and attenuation challenges, thereby allowing higher-resolution imaging deep into the cortex.

Previous studies have shown that minimal neural damage was induced by the microprism implantation [25–28]. However, the microcirculatory changes post prism implantation have not been investigated. According to our model, the circulation of the superficial layer was slightly affected during the first several days with cortical bleeding and inflammation being the main issue. It is reasonable to expect that the deep cortical vessels suffer more severe damage due to direct cutting, involving tissue damage, edema, and bleeding. However, the vessel morphology, vessel density and vessel diameter measurements obtained from the side-view vis-OCTA demonstrate recovery after 15 days following prism implantation. This observation suggests that waiting for at least two weeks following microprism implantation surgery is necessary for the brain to fully stabilize.

We also compared the long-term optical qualities through the combined prism and cranial window and through the cranial window only. The microscopic image quality through the prism is comparable to the adjacent area without prism, and the vis-OCT *en face* image also shows similar resolution both through and without the microprism. In addition, our results demonstrate that the microprism and cranial window remained completely transparent through the entire 60 days after implantation, which is especially important for longitudinal investigation. To achieve such long-term stable optical quality, several techniques were used in our animal preparation. First, we removed the dura to prevent fibrosis on the brain surface and subsequent blurring of the chronic cranial window. Second, by adding a small drop of removable optical glue on the coverslip to prevent dust and scratches, the image window surface remained clean throughout the

duration of the longitudinal monitoring. Third, the cover glass was firmly attached to the brain surface, which can both reduce post-surgical bleeding for better imaging quality and prevent fluid accumulation between the brain and the window.

Using the tMCAO model, we successfully investigated the acute and chronic dynamic circulatory changes of both the deep cortex from the side view and superficial cortex from the top-view. During the first three days of the acute stage, vis-OCTA reveals that the deep cortex is more severely ischemic than the superficial cortex. Longitudinal monitoring through both the side-view and top-view vis-OCTA further demonstrated the different patterns of vessel density changes in deep and superficial cortex. This result is concordant with the phenomenon that degree of increased vessel density is related to the severity of ischemic area [41]. From the side view, it also appears that the degree of increased vessel density is lower in the deep cortical region adjacent to the white matter, which coincides with the fact that the cortex has much higher vessel density and oxygen requirement than the white matter, resulting in different responses to ischemic stress [42–44].

There are a few limitations in our experiment. First, although the brain damage by prism implantation is considered acceptable, there are still potential permanent influences to the brain structure and functions that need to be further investigated. Second, the microprism enlarged the imaging depth by imaging though the side, but the thickness of the side-view volume (Fig. 2e) is still limited by optical scattering in the brain. Third, the bleeding on the surface of the brain that was present the first few days after implantation may have affected measurements of vessel density and dilation. The high absorption of blood may block signal from vessels beneath the pooling blood, artificially decreasing vessel density measurements in those first 7 days following implantation. However, OCTA signal from blood vessels can still be clearly observed even under liquid accumulation in angiographic B-scans. Additionally, the vessel dilation occurs in the side view on days 2 and 3 after implantation, even when there is no fluid visible in the B-scans (Figs. 4e1 and 4e2). Similarly, in the top view, the vessel dilation was more significant on day 3 than day 7, while there is greater fluid accumulation on day 7. The presence and amount of fluid does not appear to be correlated to vessel dilation after implantation. The identity of the pooled fluid in Fig. 4 needs further investigation, but its optical properties are consistent with that of cerebrospinal fluid.

Additionally, we acknowledge that our quantitative vessel dilation measurements need a better baseline comparison. This is because implanting a cranial window has been shown to causes acute vasodilation [45]. However, our findings of approximately 2 weeks to recovery are consistent with previously published findings of implanted cranial window without prism, where large and medium vessels require approximately 3–4 weeks to recover [45]. We also acknowledge that without histological evidence or other whole brain imaging such as MRI, we can only speculate as to why the field of view shifted significantly between days 3 and 30 post stroke (Fig. 6). The timeline of this change is consistent with both the replacement of the necrotic core of the infarction with a growing fluid filled cavity at day 21 post stroke [38] and also with increased ventricle size at day 30 post stroke [37]. Both of those changes could be responsible for distorting the brain tissue at the location we imaged through the prism.

Finally, our current experiment focuses on the structural and circulatory changes only. Many other areas of functional information are yet to be explored. One future step is to combine this microprism implantation with vis-OCT oxygen saturation measurements to explore ischemic stroke in both superficial and deep cortex. Another future goal is to integrate vis-OCT, fluorescence microscopy, and microprism to collectively investigate structural and functional changes such as neural morphology, oxygen tension, and blood flow [46].

5.   Conclusion

In conclusion, we present a vis-OCT imaging system that imaged the entire brain cortex through a cranial window integrated with a microprism. This method allows for *in vivo*, high-quality vis-OCT imaging of murine cortex for 60 days. It provides a new modality to simultaneously investigate both superficial and deep cortex. Using vis-OCT, we wish to better understand the structural and functional changes of cerebrovascular disease and eventually develop a translatable outcome measure for therapeutic interventions.

Funding

Disclosures

C. Sun and H. F. Zhang have financial interests in Opticent Health, which did not support this work. Other authors declare that there are no conflicts of interest related to this article.

References

1. J. H. Chin and N. Vora, "The global burden of neurologic diseases," Neurology **83**(4), 349–351 (2014).
2. J. Liu, "Post stroke angiogenesis: Blood, bloom or brood," Stroke **46**(5), e105–e106 (2015).
3. E. Cuccione, G. Padovano, A. Versace, C. Ferrarese, and S. Beretta, "Cerebral collateral circulation in experimental ischemic stroke," Exp. Transl. Stroke Med. **8**(1), 2 (2016).
4. A. Sigler and T. H. Murphy, "In vivo 2-photon imaging of fine structure in the rodent brain: before, during, and after stroke," Stroke **41**(10, Supplement 1), S117–S123 (2010).
5. X. Shu, L. J. Beckmann, and H. F. Zhang, "Visible-light optical coherence tomography: a review," J. Biomed. Opt. **22**(12), 1–14 (2017).
6. W. Liu, S. Wang, B. Soetikno, J. Yi, K. Zhang, S. Chen, R. A. Linsenmeier, C. M. Sorenson, N. Sheibani, and H. F. Zhang, "Increased Retinal Oxygen Metabolism Precedes Microvascular Alterations in Type 1 Diabetic Mice," Invest. Ophthalmol. Visual Sci. **58**(2), 981–989 (2017).
7. S. Pi, A. Camino, W. Cepurna, X. Wei, M. Zhang, D. Huang, J. Morrison, and Y. Jia, "Automated spectroscopic retinal oximetry with visible-light optical coherence tomography," Biomed. Opt. Express **9**(5), 2056–2067 (2018).
8. B. T. Soetikno, L. Beckmann, X. Zhang, A. A. Fawzi, and H. F. Zhang, "Visible-light optical coherence tomography oximetry based on circumpapillary scan and graph-search segmentation," Biomed. Opt. Express **9**(8), 3640–3652 (2018).
9. B. T. Soetikno, J. Yi, R. Shah, W. Liu, P. Purta, H. F. Zhang, and A. A. Fawzi, "Inner retinal oxygen metabolism in the 50/10 oxygen-induced retinopathy model," Sci. Rep. **5**(1), 16752 (2015).
10. J. Yi, W. Liu, S. Chen, V. Backman, N. Sheibani, C. M. Sorenson, A. A. Fawzi, R. A. Linsenmeier, and H. F. Zhang, "Visible light optical coherence tomography measures retinal oxygen metabolic response to systemic oxygenation," Light: Sci. Appl. **4**(9), e334 (2015).
11. J. Yi, Q. Wei, W. Liu, V. Backman, and H. F. Zhang, "Visible-light optical coherence tomography for retinal oximetry," Opt. Lett. **38**(11), 1796–1798 (2013).
12. S. P. Chong, T. Zhang, A. Kho, M. T. Bernucci, A. Dubra, and V. J. Srinivasan, "Ultrahigh resolution retinal imaging by visible light OCT with longitudinal achromatization," Biomed. Opt. Express **9**(4), 1477–1491 (2018).
13. J. Yi, S. Chen, X. Shu, A. A. Fawzi, and H. F. Zhang, "Human retinal imaging using visible-light optical coherence tomography guided by scanning laser ophthalmoscopy," Biomed. Opt. Express **6**(10), 3701–3713 (2015).
14. S. Chen, X. Shu, P. L. Nesper, W. Liu, A. A. Fawzi, and H. F. Zhang, "Retinal oximetry in humans using visible-light optical coherence tomography [Invited]," Biomed. Opt. Express **8**(3), 1415–1429 (2017).
15. S. Chen, Q. Liu, X. Shu, B. Soetikno, S. Tong, and H. F. Zhang, "Imaging hemodynamic response after ischemic stroke in mouse cortex using visible-light optical coherence tomography," Biomed. Opt. Express **7**(9), 3377–3389 (2016).
16. S. P. Chong, C. W. Merkle, C. Leahy, H. Radhakrishnan, and V. J. Srinivasan, "Quantitative microvascular hemoglobin mapping using visible light spectroscopic Optical Coherence Tomography," Biomed. Opt. Express **6**(4), 1429–1450 (2015).
17. S. P. Chong, C. W. Merkle, C. Leahy, and V. J. Srinivasan, "Cerebral metabolic rate of oxygen (CMRO(2)) assessed by combined Doppler and spectroscopic OCT," Biomed. Opt. Express **6**(10), 3941–3951 (2015).
18. A. Lichtenegger, D. J. Harper, M. Augustin, P. Eugui, M. Muck, J. Gesperger, C. K. Hitzenberger, A. Woehrer, and B. Baumann, "Spectroscopic imaging with spectral domain visible light optical coherence microscopy in Alzheimer's disease brain samples," Biomed. Opt. Express **8**(9), 4007–4025 (2017).

19. V. J. Srinivasan, E. T. Mandeville, A. Can, F. Blasi, M. Climov, A. Daneshmand, J. H. Lee, E. Yu, H. Radhakrishnan, E. H. Lo, S. Sakadžić, K. Eikermann-Haerter, and C. Ayata, "Multiparametric, Longitudinal Optical Coherence Tomography Imaging Reveals Acute Injury and Chronic Recovery in Experimental Ischemic Stroke," PLoS One **8**(8), e71478 (2013).

20. Q. Liu, S. Chen, B. Soetikno, W. Liu, S. Tong, and H. Zhang, "Monitoring acute stroke in mouse model using laser speckle imaging-guided visible-light optical coherence tomography," IEEE Trans. Biomed. Eng. **65**(10), 2136–2142 (2018).

21. A. N. Yaroslavsky, P. C. Schulze, I. V. Yaroslavsky, R. Schober, F. Ulrich, and H. J. Schwarzmaier, "Optical properties of selected native and coagulated human brain tissues in vitro in the visible and near infrared spectral range," Phys. Med. Biol. **47**(12), 2059–2073 (2002).

22. A. Ergul, A. Alhusban, and S. C. Fagan, "Angiogenesis: A Harmonized Target for Recovery after Stroke," Stroke **43**(8), 2270–2274 (2012).

23. D. Navaratna, S. Guo, K. Arai, and E. H. Lo, "Mechanisms and targets for angiogenic therapy after stroke," Cell Adhes. Migr. **3**(2), 216–223 (2009).

24. Y. Jia, M. R. Grafe, A. Gruber, N. J. Alkayed, and R. K. Wang, "In vivo optical imaging of revascularization after brain trauma in mice," Microvasc. Res. **81**(1), 73–80 (2011).

25. M. L. Andermann, N. B. Gilfoy, G. J. Goldey, R. N. S. Sachdev, M. Wölfel, D. A. McCormick, R. C. Reid, and M. J. Levene, "Chronic cellular imaging of entire cortical columns in awake mice using microprisms," *Neuron* 80, (2013).

26. T. H. Chia and M. J. Levene, "Microprisms for In Vivo Multilayer Cortical Imaging," J. Neurophysiol. **102**(2), 1310–1314 (2009).

27. T. H. Chia and M. J. Levene, "Multi-Layer In Vivo Imaging of Neocortex Using a Microprism," Cold Spring Harb Protoc **2010**(8), pdb.prot5476 (2010).

28. T. H. Chia and M. J. Levene, "In vivo Imaging of Deep Cortical Layers using a Microprism," *J. Visualized Exp.* (30), 1509 (2009).

29. J. A. Izatt, M. A. Choma, and A.-H. Dhalla, "Theory of Optical Coherence Tomography," in *Optical Coherence Tomography: Technology and Applications*, W. Drexler and J. G. Fujimoto, eds. (Springer International Publishing, Cham, 2015), pp. 65–94.

30. N. Lue, J. Bewersdorf, M. D. Lessard, K. Badizadegan, R. R. Dasari, M. S. Feld, and G. Popescu, "Tissue refractometry using Hilbert phase microscopy," Opt. Lett. **32**(24), 3522–3524 (2007).

31. N. Percie du Sert, A. Alfieri, S. M. Allan, H. V. Carswell, G. A. Deuchar, T. D. Farr, P. Flecknell, L. Gallagher, C. L. Gibson, M. J. Haley, M. R. Macleod, B. W. McColl, C. McCabe, A. Morancho, L. D. Moon, M. J. O'Neill, I. Pérez de Puig, A. Planas, C. I. Ragan, A. Rosell, L. A. Roy, K. O. Ryder, A. Simats, E. S. Sena, B. A. Sutherland, M. D. Tricklebank, R. C. Trueman, L. Whitfield, R. Wong, and I. M. Macrae, "The IMPROVE Guidelines (Ischaemia Models: Procedural Refinements Of in Vivo Experiments)," J. Cereb. Blood Flow Metab. **37**(11), 3488–3517 (2017).

32. O. Engel, S. Kolodziej, U. Dirnagl, and V. Prinz, "Modeling Stroke in Mice - Middle Cerebral Artery Occlusion with the Filament Model," *J. Visualized Exp.* (47), 2423 (2011).

33. C. A. Schneider, W. S. Rasband, and K. W. Eliceiri, "NIH Image to ImageJ: 25 years of image analysis," Nat. Methods **9**(7), 671–675 (2012).

34. E. Zudaire, L. Gambardella, C. Kurcz, and S. Vermeren, "A Computational Tool for Quantitative Analysis of Vascular Networks," PLoS One **6**(11), e27385 (2011).

35. C. W. Merkle, J. Zhu, M. T. Bernucci, and V. J. Srinivasan, "Dynamic Contrast Optical Coherence Tomography reveals laminar microvascular hemodynamics in the mouse neocortex in vivo," NeuroImage **202**, 116067 (2019).

36. "Allen Mouse Brain Atlas. http://mouse.brain-map.org/static/atlas."

37. M. A. Mirza, L. A. Capozzi, Y. Xu, L. D. McCullough, and F. Liu, "Knockout of vascular early response gene worsens chronic stroke outcomes in neonatal mice," Brain Res. Bull. **98**, 111–121 (2013).

38. S. S. J. Rewell, L. Churilov, T. K. Sidon, E. Aleksoska, S. F. Cox, M. R. Macleod, and D. W. Howells, "Evolution of ischemic damage and behavioural deficit over 6 months after MCAo in the rat: Selecting the optimal outcomes and statistical power for multi-centre preclinical trials," PLoS One **12**(2), e0171688 (2017).

39. T. G. Belgard, A. C. Marques, P. L. Oliver, H. O. Abaan, T. M. Sirey, A. Hoerder-Suabedissen, F. García-Moreno, Z. Molnár, E. H. Margulies, and C. P. Ponting, "A transcriptomic atlas of mouse neocortical layers," Neuron **71**(4), 605–616 (2011).

40. S. P. Chong, C. W. Merkle, D. F. Cooke, T. Zhang, H. Radhakrishnan, L. Krubitzer, and V. J. Srinivasan, "Noninvasive, in vivo imaging of subcortical mouse brain regions with 1.7 μm optical coherence tomography," Opt. Lett. **40**(21), 4911–4914 (2015).

41. T. Hayashi, K. Deguchi, S. Nagotani, H. Zhang, Y. Sehara, A. Tsuchiya, and K. Abe, "Cerebral ischemia and angiogenesis," Curr. Neurovasc. Res. **3**(2), 119–129 (2006).

42. K. A. Rempp, G. Brix, F. Wenz, C. R. Becker, F. Gückel, and W. J. Lorenz, "Quantification of regional cerebral blood flow and volume with dynamic susceptibility contrast-enhanced MR imaging," Radiology **193**(3), 637–641 (1994).

43. D. L. Adams, V. Piserchia, J. R. Economides, and J. C. Horton, "Vascular Supply of the Cerebral Cortex is Specialized for Cell Layers but Not Columns," Cereb. Cortex **25**(10), 3673–3681 (2015).

44. P. S. Tsai, J. P. Kaufhold, P. Blinder, B. Friedman, P. J. Drew, H. J. Karten, P. D. Lyden, and D. Kleinfeld, "Correlations of neuronal and microvascular densities in murine cortex revealed by direct counting and colocalization of nuclei and vessels," J. Neurosci. **29**(46), 14553–14570 (2009).

45. D. X. Hammer, A. Lozzi, E. Abliz, N. Greenbaum, A. Agrawal, V. Krauthamer, and C. G. Welle, "Longitudinal vascular dynamics following cranial window and electrode implantation measured with speckle variance optical coherence angiography," Biomed. Opt. Express **5**(8), 2823–2836 (2014).

46. I. Perez-de-Puig, F. Miró-Mur, M. Ferrer-Ferrer, E. Gelpi, J. Pedragosa, C. Justicia, X. Urra, A. Chamorro, and A. M. Planas, "Neutrophil recruitment to the brain in mouse and human ischemic stroke," Acta Neuropathol. **129**(2), 239–257 (2015).